Numerical simulation of Ar-x%CO$_2$ shielding gas and its effect on an electric welding arc

Isabelle Choquet[1], Håkan Nilsson[2], Alireza Javidi Shirvan[1], Nils Stenbacka[1]

[1]University West, Department of Engineering Science, Trollhättan, Sweden,

[2]Chalmers University of Technology, Department of Applied Mechanics, Gothenburg, Sweden

isabelle.choquet@hv.se

ABSTRACT

This study focuses on the simulation of a plasma arc heat source in the context of electric arc welding. The simulation model was implemented in the open source CFD software OpenFOAM-1.6.x, in three space dimensions, coupling thermal fluid mechanics with electromagnetism. Two approaches were considered for calculating the magnetic field: i) the three-dimensional approach, and ii) the so-called axisymmetric approach. The electromagnetic part of the solver was tested against analytic solution for an infinite electric rod. Perfect agreement was obtained. The complete solver was tested against experimental measurements for Gas Tungsten Arc Welding (GTAW) with an axisymmetric configuration. The shielding gas was argon, and the anode and cathode were treated as boundary conditions. The numerical solutions then depend significantly on the approach used for calculating the magnetic field. The so-called axisymmetric approach indeed neglects the radial current density component, mainly resulting in a poor estimation of the arc velocity. Plasma arc simulations were done for various Ar-x%CO$_2$ shielding gas compositions: pure argon (x=0), pure carbon dioxide (x=100), and mixtures of these two gases with x=1 and 10% in mole. The simulation results clearly show that the presence of carbon dioxide results in thermal arc constriction, and increased maximum arc temperature and velocity. Various boundary conditions were set on the anode and cathode (using argon as shielding gas) to evaluate their influence on the plasma arc. These conditions, difficult to measure and to estimate a priori, significantly affect the heat source simulation results. Solution of the temperature and electromagnetic fields in the anode and cathode will thus be included in the forthcoming developments.

Keywords: electric arc welding, electric heat source, thermal plasma, magnetic potential, inert gas, active gas, spatial distribution of thermal energy, GTAW, TIG, WIG.

1 INTRODUCTION

Man made electric arc was first produced in 1800 by Sir Humphry Davy using carbon electrodes. Electric arc welding as a method of assembling metal parts through fusion was however initiated much later, at the end of the 19's century, when C.L. Coffin introduced metal electrode and metal transfer across an arc. Thanks to intense developments in the early 1900's, such as the first coated electrode developed by A.P. Strohmenger and O. Kjellberg, electric arc welding started being utilized in production in the 1920's, and then in large scale production from the 1930's.

This manufacturing process, although used since many decades, is still under intensive development, in order to further improve different aspects such as process productivity, process control, and weld qual-

ity. Such improvements are beneficial both from economical and environmental sustainability. Electric arc welding is interdisciplinary in nature, and complex to master as it involves very large temperature gradients, and a number of parameters that do interact in a nonlinear way. Its investigation was long based on experimental studies. Today, thanks to recent and significant progress done in the field of welding simulation, experiments can be complemented with numerical modeling to reach a deeper process understanding. As an illustration, the change in microstructure can be simulated for a given thermal history within the heat affected zone of the base metal, as in [1]. The numerical calculation of the residual stresses, to investigate fatigue and distortion, can now be coupled with the weld pool as in [2], calibrating functional approximations of volume and surface heat flux transferred from the electric arc.

Electric arcs used in welding are generally formed coupling an electric discharge between anode and cathode with a gas flow. A main goal is to form a shielding gas flow characterized by temperatures large enough to melt the materials to be welded, i.e. a thermal plasma flow. The numerical modeling of a thermal plasma flow is thus a base element for characterising the thermal history of an electric arc welding process, by calculating the thermal energy provided to the parent metal, and its spatial distribution.

A thermal plasma is basically modeled coupling thermal fluid mechanics (governing mass, momentum and energy or enthalpy) with electromagnetism (governing the electric field, the magnetic field, and the current density). Different thermal plasma models can be found in the literature in the context of electric arc welding simulation. They were developed to address in more detail various aspects of electric arc welding heat source. As an illustration, a simulation model for axisymmetric configuration, describing consistently the arc core, the arc sheath (or arc/anode and arc/cathode boundary), and the solid electrodes was developed in [3], and applied to Gas Tungsten Arc Welding (GTAW). Other models account for thermal non-equilibrium [4], or for the influence of metal vapour on the thermodynamic and transport properties of a plasma arc [5]. Coupled arc and weld pool simulation tools were recently developed for axisymmetric configuration [6], without considering the plasma arc sheath. At least one of these coupled arc-

pool simulation tools also account for 3-dimensional effects and arc dynamic behavior [7].

The numerical modeling of the thermal plasma heat source within the frame of electric arc welding started only recently in Sweden. The rigorous derivation of a fluid arc model was done in [8], based on kinetic theory. This plasma arc model was derived from a system of Boltzmann type transport equations. A viscous hydrodynamic/diffusion limit was obtained in two stages doing an Hilbert expansion and using the Chapman-Enskog method. The resultant viscous fluid model is characterized by two temperatures, and non equilibrium ionization. It applies to the arc plasma core and the ionization zone of the arc plasma sheath. The development of a numerical tool for simulating a thermal plasma arc was initiated in [9]. The present study is in the continuation of [9]. The model implemented in this first stage is a simplified version of the model derived in [8], as it assumes local thermal equilibrium, applies to the plasma core and does not consider the arc plasma sheath. The implementation was done in the open source CFD software OpenFOAM-1.6.x (www.openfoam.com), considering three space dimensions. OpenFOAM was distributed as OpenSource in 2004. This simulation software is a C++ library of object-oriented classes that can be used for implementing solvers for continuum mechanics. It includes a number of solvers for different continuum mechanical problems. Due to the availability of the source code, its libraries can be used to implement new solvers for other applications. The current implementation is based on the buoyantSimpleFoam solver, which is a steady-state solver for buoyant, turbulent flow of compressible fluids. The partial differential equations of this solver are discretized using the finite volume method. The thermal plasma simulation model implemented in OpenFOAM-1.6.x is described in section 2. It couples a simplified system of Maxwell equations (section 2.1) with a system of thermal Navier-Stokes equations in three space-dimensions (section 2.2). Two approaches were considered for calculating the magnetic field:

   i) the three-dimensional approach, and

   ii) a so-called axisymmetric approach,

as detailed in section 2.1.

The electromagnetic part of the solver was tested against analytic solution for an infinite electric rod. The test case and the results are presented in section 3.1.

The complete solver was tested against experimental measurements for GTAW available in the literature. The experimental configuration was axisymmetric, and the shielding gas was argon. The anode and cathode were treated as boundary conditions in the simulations. This second test case, and the related simulation results, are presented in section 3.2. For each test case both approaches for calculating the magnetic field were used, and the validity of the simplified (or so-called axisymmetric) version are discussed. Plasma arc simulations with the three dimensional approach for calculating the magnetic field, were also done for various Ar-x%CO_2 shielding gas compositions. The simulation results of the following four cases are reported and discussed in section 3.3: pure argon (x=0), pure carbon dioxide (x=100), and mixtures of these two gases with x=1 and 10% in mole. The influence of the boundary conditions (set on the anode and cathode) on the arc temperature and velocity were investigated using the three dimensional approach for calculating the magnetic field, and retaining argon as shielding gas. The corresponding simulation results are presented and discussed in section 3.4. The main results and conclusions are summarised in section 4.

2   MODEL

The model described below is a first step in the development of a simulation tool for thermal plasma arc applied to electric arc welding. In this first stage, the model describes an arc plasma core, and thus assumes local thermal equilibrium. The arc plasma sheat is not included. The implementation was done in the open source CFD software OpenFOAM-1.6.x (www.openfoam.com), considering three space dimensions, and coupling thermal fluid mechanics with electromagnetism. The fluid and electromagnetic models are tightly coupled. The Lorentz force, or magnetic pinch force, resulting from the induced magnetic field indeed acts as the main cause of plasma flow acceleration. The Joule heating because of the electric field is the largest heat source governing the plasma energy (and thus temperature). On the other hand the system of equations governing electromagnetism is temperature dependent, via the electric conductivity. The main specificities of the implemented electromagnetic and thermal fluid model are as follow.

2.1   Electromagnetic model

The electromagnetic component of the model is derived from the Maxwell equations (see [9] for further derivation details), assuming:
- a Debye length λ_D much smaller than the characteristic length of the welding arc, thus local electro-neutrality in the plasma core,
- characteristic time and length of the welding arc allowing neglecting the convection current compared to the conduction current in Ampere's law, resulting in quasi-steady electromagnetic phenomena,
- a Larmor frequency much smaller than the average collision frequency of electrons, implying a negligible Hall current compared to the conduction current, and
- a magnetic Reynolds number much smaller than unity, leading to a negligible induction current compared to the conduction current.
Then, the electric potential V is governed by the Laplace equation,

$$\nabla \cdot [\sigma(T) \, \nabla V] = 0 \, , \qquad (1)$$

where T is the temperature, ∇ denotes the gradient operator, and $\nabla \cdot$ the divergence operator. The electric conductivity $\sigma(T)$ is temperature dependent, as illustrated in Fig.1 for an argon plasma.
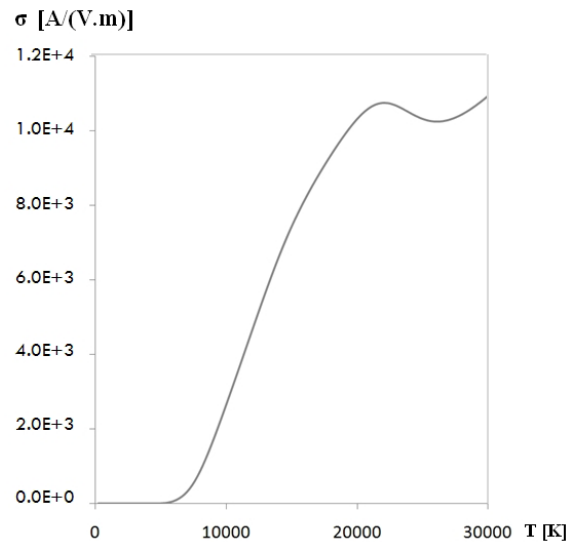

Figure 1: Argon plasma electric conductivity as function of temperature.

The electric field $\vec{E}$, is defined from the gradient of the electric potential,

$$\vec{E} = -\nabla V . \qquad (2)$$

The electric current density $\vec{J}$ is given by Ohm's law,

$$\vec{J} = -\sigma(T)\,\nabla V . \qquad (3)$$

Two approaches are used in this paper for calculating the magnetic field, $\vec{B}$. One of them computes the magnetic potential field $\vec{A}$ in 3-space dimensions, Eq. (4), and from that the magnetic field, Eq. (5). While the other, called axisymmetric approach, computes only one component of the magnetic field, Eq. (6).

The magnetic potential $\vec{A}$ is governed by the Poisson equation,

$$\triangle\vec{A} = \sigma(T)\,\mu_o\,\nabla V , \qquad (4)$$

where $\triangle$ denotes the Laplace operator, and μ_o the permeability of free space. The magnetic field $\vec{B}$ is defined in 3-space dimensions as the rotational of the magnetic potential,

$$\vec{B} = \nabla \times \vec{A} , \qquad (5)$$

where $\nabla \times$ denotes the rotational operator.

For axisymmetric configurations the calculation of the magnetic field, Eqs. (4)-(5), is often reduced to the single angular component

$$B_\theta(r) = \frac{\mu_o}{r}\int_0^r J_{axial}(l)\,l\,dl , \qquad (6)$$

where r is the radial distance to the symmetry axis, and J_{axial} the axial component of the current density. Notice that this simplified expression is obtained doing an additional assumption sometimes omitted: the current density vector is axial, that is aligned with the direction of the symmetry axis. So axisymmetric configurations should also be invariant by translation along the symmetry axis to satisfy this additional condition. Such a simplification can be used for investigating long arcs, as done by Hsu and co-authors in [10]. Tsai and co-authors underlined in [11] that this simplification may need to be questioned for short arcs. The arcs used in electric arc welding use to be short.

2.2 Fluid model

The thermal fluid component of the model applies to a Newtonian and thermally expansible fluid, assuming:
- a one-fluid model,
- in local thermal equilibrium, and
- mechanically incompressible, because of the small Mach number.
- the flow is steady-state and laminar, which is specified using the option of laminar flow in the OpenFOAM turbulence model class.

The model is thus suited to the plasma core. The treatment of the plasma sheath would require a two-fluid model with partial thermal equilibrium, to account for electron diffusion, and for the temperature difference observed between electrons and heavy particles in the plasma arc sheath.

In the present framework, and with steady-state conditions, the continuity equation is written as

$$\nabla \cdot [\rho(T)\,\vec{u}] = 0 , \qquad (7)$$

where ρ denotes the fluid density, and $\vec{u}$ the fluid velocity. The density $\rho(T)$ is here temperature dependent, as illustrated for argon plasma in Fig. 2.
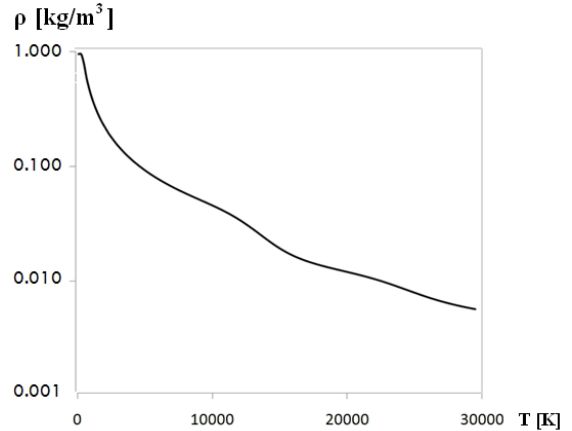

Figure 2: Argon plasma density as function of temperature.

The momentum conservation equation is expressed as

$$\nabla \cdot [\,\rho(T)\,\vec{u} \otimes \vec{u}\,] - \vec{u}\,\nabla \cdot [\rho(T)\,\vec{u}]$$
$$-\nabla \cdot [\mu(T)\left(\nabla\vec{u} + (\nabla\vec{u})^T\right) - \tfrac{2}{3}\,\mu(T)\,(\nabla \cdot \vec{u})I]$$
$$= -\nabla P + \vec{J} \times \vec{B} , \qquad (8)$$

where the operators $\otimes$ and $\times$ denote the tensorial and vectorial product, respectively. I is the identity tensor, μ the viscosity, and P the pressure. The last term on the right hand side of Eq. (8) is the Lorentz force. The enthalpy conservation equation is

$$\nabla \cdot [\rho(T)\vec{u}\ h] - h\,\nabla \cdot [\rho(T)\,\vec{u}] - \nabla \cdot [\alpha(T)\,\nabla h]$$

$$= \nabla \cdot (\vec{u}\,P) - P\,\nabla \cdot \vec{u} + \vec{J} \cdot \vec{E}$$

$$-Q_{rad} + \nabla \cdot \Big[\frac{5\,k_B\,\vec{J}}{2\,e\,C_p(T)}\,h\Big]\,, \tag{9}$$

where h is the specific enthalpy, α is the thermal diffusivity, Q_{rad} the radiation heat loss, k_B the Boltzmann constant, e the elementary charge, and C_p the specific heat at constant pressure. The third term on the right hand side of Eq. (9) is the Joule heating, and the last term the transport of electron enthalpy. The temperature, T, is derived from the specific enthalpy via the definition of the specific heat,

$$C_p(T) = \Big(\frac{dh}{dT}\Big)_P\,, \tag{10}$$

which is plotted in Fig. 3 for Ar and CO_2 plasma.
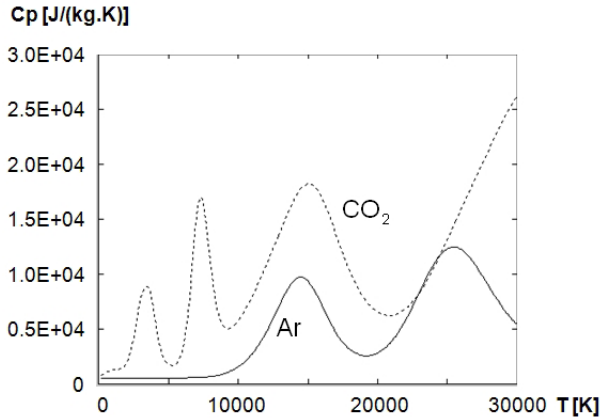
Figure 3: Specific heat as function of temperature for Ar (solid line) and CO_2 (dotted line).

The thermodynamic and transport properties are linearly interpolated from tabulated data implemented on a temperature range from 200 to 30 000 K, with a temperature increment of 100 K. These data tables were derived for an argon plasma [12], and a carbon dioxide plasma [13], using kinetic theory.

3 TEST CASES

Two test cases were considered. The first one, an infinite rod, was retained since it has an analytic solution allowing testing the electromagnetic part of the simulation model, and the two calulation methods for the magnetic field. The second is the water cooled GTAW test case described in [11]. It was investigated experimentally in [14], and used in the literature as reference case for testing arc heat source simulation models.

3.1 Infinite rod

The magnetic field induced in and around an infinite rod of radius r_o with constant electric conductivity, and constant current density parallel to the rod axis, reduces to an angular component B_θ with the following analytic expression (see [9] for further details):

$$B_\theta(r) = \frac{\mu_o J_{axial}\,r}{2} \quad if \quad r < r_o\,,$$

$$B_\theta(r) = \frac{\mu_o J_{axial}\,r_o^2}{2\,r} \quad if \quad r \geq r_o\,. \tag{11}$$

$J_{axial} = I/(\pi\,r_o)$ denotes the current density along the rod axis, and I the current intensity.
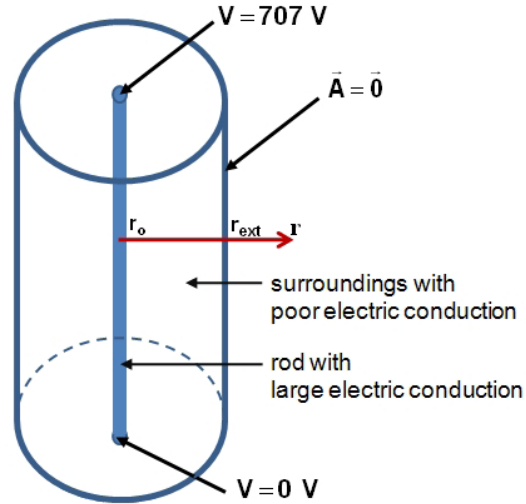

Figure 4: Schematic representation of the computational domain.

A long rod of radius $r_o = 1$ mm with the large and uniform electric conductivity $\sigma_{rod} = 2700 A/(Vm)$,

surrounded by a poor conducting region of radius r_{ext} = 16 mm, and uniform electric conductivity σ_{sur} = $10^{-5} A/(Vm)$, was simulated. Notice that the conductivity σ_{rod} and σ_{sur} correspond to an argon plasma at 10600 and 300 K, respectively.

The electric potential difference applied on the rod was set to 707 V, as indicated in Fig. 4. It corresponds here to a current intensity of 600 A. The electric potential gradient along the direction normal to the boundary was set to zero on all the other boundaries.

The magnetic field was calculated using both the i) three-dimensional approach, Eqs. (4)-(5), and the ii) axisymmetric approach, Eq. (6). In the three-dimensional approach, the magnetic potential $\vec{A}$ was set to zero at $r = r_{ext}$, and its gradient along the direction normal to the boundary was set to zero on all the other boundaries.

The calculation results, plotted in Fig. 5 for the angular component of the magnetic field, are both in perfect agreement with the analytic solution, as expected when the current density is aligned with the symmetry axis.
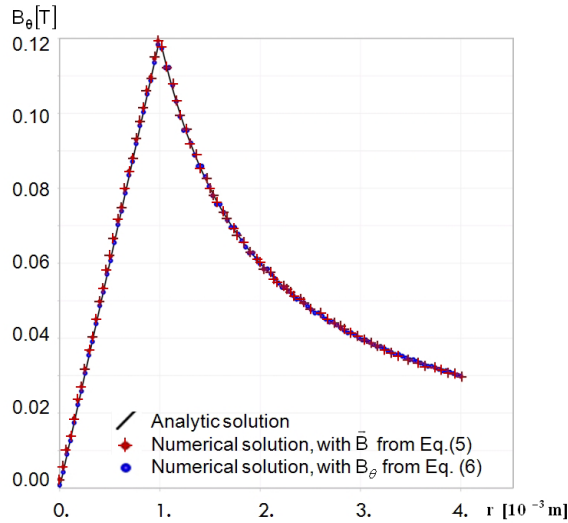
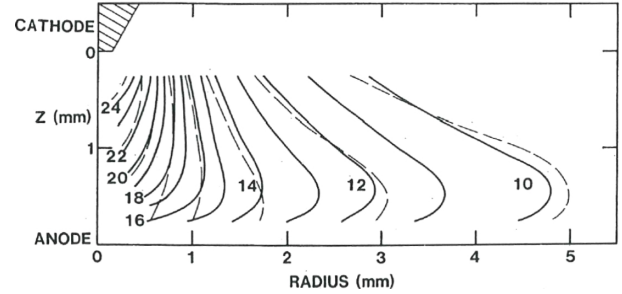ported in Fig. 6, is now considered.

Figure 6: Temperature measurements of [14].

The configuration is sketched Fig. 7. The electrode, of radius 1.6 mm, has a conical tip of angle 60° truncated at a tip radius of 0.5 mm. The electrode is mounted inside a ceramic nozzle of internal and external radius 5 mm and 8.2 mm, respecively. The pure argon shielding gas enters the nozzle at room temperature and at an average mass flow rate of $1.66 \cdot 10^{-4}$ m³/s.
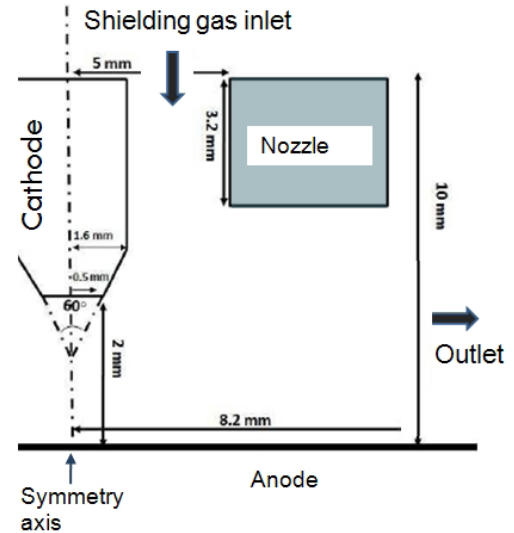

Figure 5: Angular component of the magnetic field along the radial direction ($r_o = 1 \times 10^{-3}$m).

Figure 7: Schematic representation of the GTAW test case

3.2 Water cooled GTAW with Ar shielding gas

The 2 mm long and 200 A argon arc studied in [11], based on the experimental measurements of [14] re-

The temperature and the current density set on the cathode boundary are explicitly given in [11]. The anode surface temperature was also set as proposed in [11], extrapolating the experimental results of [14]. Looking at the experimental results, Fig. 6, it can be

noticed that the measured temperature is rather difficult to extrapolate up to the anode. The boundary conditions set on the cathode also suffer from a lack of accuracy, as experimental measurements could not be done in the very close vicinity of the anode and cathode. These difficulties may explain the variety of boundary conditions used in the literature for simulating this test case.
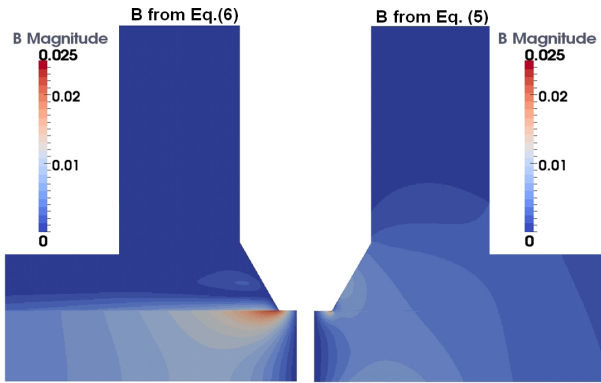

Figure 8: Magnetic field magnitude calculated with the axisymmetric (left) and the three-dimensional (right) $\vec{B}$-approach.
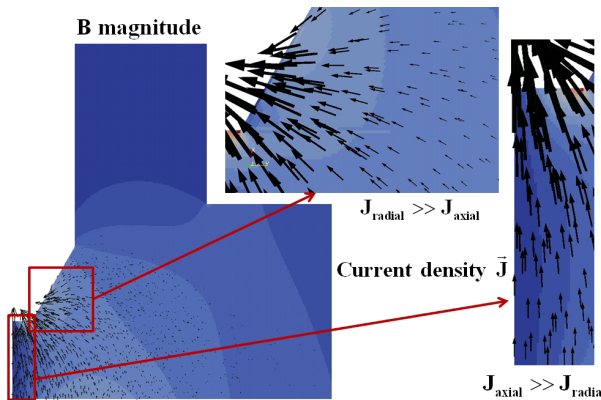
Figure 9: Current density vector calculated with the three-dimensional approach, Eqs (4)-(5) .

The simulation results presented here were calculated using 25 uniform cells along the 0.5 mm tip radius, 100 uniform cells between the electrode and parent metal along the symmetry axis, and a total number of 136250 cells. A mesh sensitivity study can be found in [15], concluding that the present mesh is sufficiently

fine. The magnetic field was calculated using both the i) three-dimensional approach, Eqs. (4)-(5), and the ii) axisymmetric approach, Eq (6). The axisymmetric approach is simpler, and often used in the literature to simulate GTAW problems. The numerical results from the two approaches significantly differ, as shown in Fig. 8. Agreement is only observed below the cathode tip, where the non-axial component of the current density is negligible compared to the axial component (see Fig. 9). The axisymmetric approach indeed neglects the radial current density component. The three-dimensional calculation, Fig. 9, shows that the non-axial component of the current density is not everywhere negligible, in particular next to the electrode tip, where the largest induced magnetic field is observed. Neglecting the non-axial component of the current density would first of all result in a poor estimation of the magnetic pinch forces, and in turn of the arc velocity, as well as the pressure force the arc exerts on the base metal. Consequently, the so-called axisymmetric approach was not retained for simulating this axisymmetric GTAW configuration.

The next simulation results were all obtained with the three-dimensional approach, Eqs (4)-(5).
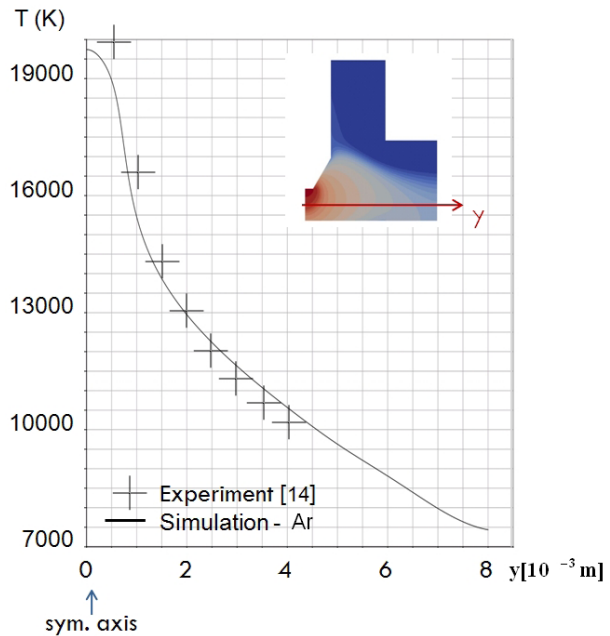

Figure 10: Temperature along the radial direction, 1 mm above the anode.

The calculated temperature is plotted along the radial direction 1 mm above the anode in Fig. 10, and along the symmetry axis in Fig. 11 (solid line). The experimental data available in [14] and shown in Fig. 6 are used for comparison with the numerical results along the radial direction, in Fig. 10. A good agreement is obtained. The comparison along the symmetry axis is difficult to perform, as the isotherms represented in Fig. 6 are not plotted in this area. We can however observe that the maximum temperature obtained numerically seems to underestimate the experimental one by about 10%. This could be due to the boundary conditions set on the anode and cathode. Other boundary conditions also used in the literature are investigated in section 3.4.

3.3 Ar-x%CO$_2$ shielding gas

Plasma arc simulations for the test case of section 3.2 were also done changing the shielding gas composition, and retaining the four following Ar-x%CO$_2$ cases: pure argon ($x = 0$), pure carbon dioxide ($x = 100$), and mixtures of these two gases with $x = 1$% and 10% in mole. In each case the thermodynamic and transport properties of the mixture (with $0 \leq x \leq 1$) are tabulated as function of the temperature, and the tables are implemented in OpenFOAM-1.6.x as described in section 2.2. For both pure argon and pure carbon dioxide the data tables result from derivations using kinetic theory, and done in [12] and [13], respectively. For the other mixtures (with $0 < x < 1$) the data tables were prepared doing an additional calulation step, based on the related data for pure argon, pure carbon dioxide, and standard mixing laws. These mixing laws use mass concentration as weigthing factor [16] for calculating the mixture specific heat and the mixture enthaphy, while they use molar concentration as weigthing factor [17] when applied to the calculation of the mixture viscosity, mixture thermal conductivity and mixture electric conductivity.

The test cases of this section were investigated as a preliminary study for future extension of the GTAW model of section 2 to active gas welding. They should be considered as academic, for various reasons now detailed.
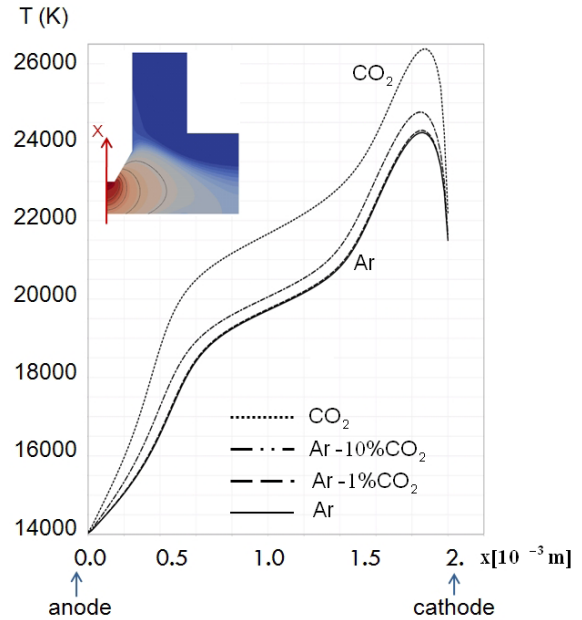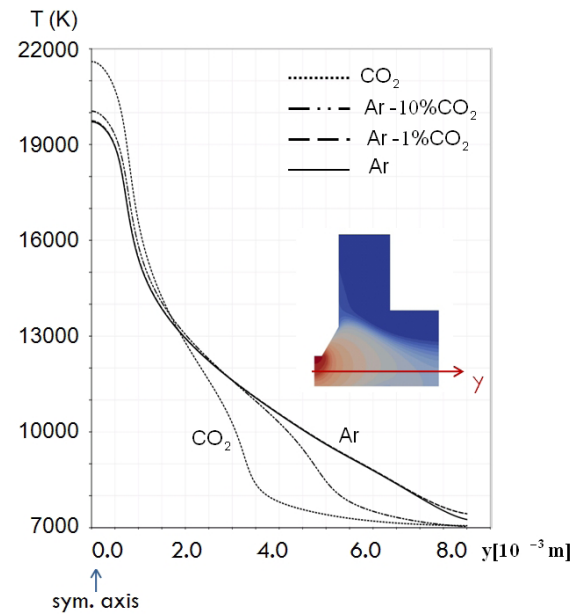

Figure 11: Temperature along the symmetry axis.

Figure 12: Temperature along the radial direction, 1 mm above the anode.
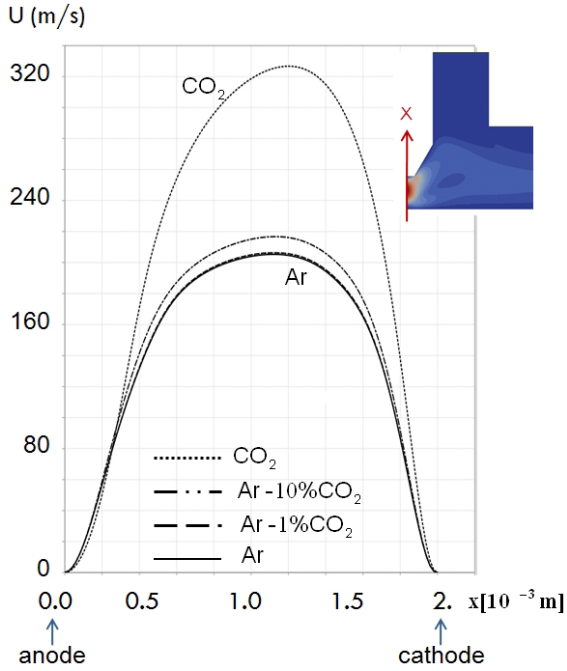
U (m/s)

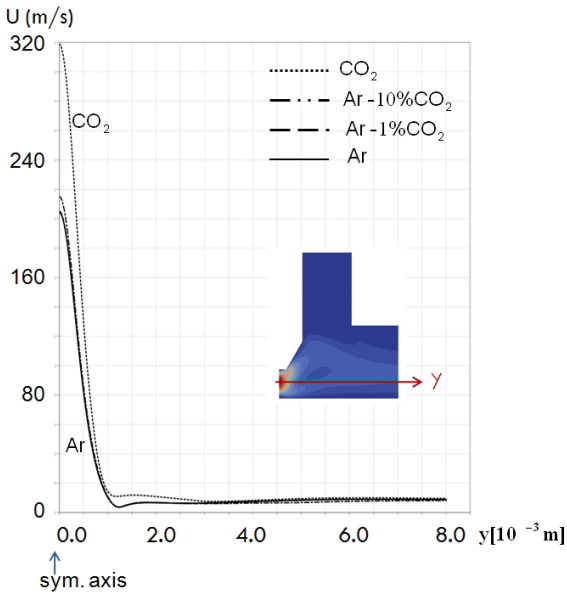**Figure 13: Velocity along the symmetry axis.**

Figure 14: Velocity along the radial direction, 1 mm above the anode.

Because of lack of experimental data, the boundary conditions set on the electrode and the base metal are the same as in section 3.2. These approximate boundary conditions are most probably oversimplified when the shielding gas contains a significant amount of CO_2. Also, the difficulty met in setting appropriate boundary conditions on the anode and cathode raises the future need of extending the simulation model coupling cathode and anode simulation to the thermal plasma arc.

The shielding gas containing x=1% in mole CO_2 should be close to the maximum amount of CO_2 allowing producing a stable electric arc with a tungsten electrode and water cooled base metal. Experiments are being prepared for characterizing this case. For a larger amount of CO_2 in the shielding gas, significant electrode oxidation is expected, leading to arc instability. A solution for making experiments feasible with a tungsten electrode could consist in shielding locally the electrode tip with an inert gas such as argon. But such a local shielding was not accounted for in the present simulations.

The present aim was to evaluate qualitatively the influence of the amount of active gas on the plasma arc temperature and velocity for given boundary conditions.

The calculated temperature is plotted along the symmetry axis in Fig. 11, and along the radial direction 1 mm above the anode in Fig. 12. In a similar way, the calculated velocity is plotted along the symmetry axis in Fig. 13, and along the radial direction 1 mm above the anode in Fig. 14. The simulation results clearly show that the presence of carbon dioxide results in an increased arc temperature (Figs. 11, 12), and a constriction of the temperature field above the base metal (Fig. 12). It also results in a significant increase of the plasma arc velocity (Figs. 13, 14), which in turn increases the pressure force applied on the base metal, but no significant change concerning the extent of the plasma jet just above the base metal (Fig. 14).

3.4 Boundary conditions

As underlined above, the available experimental measurements need to be extrapolated for estimating a priori the boundary conditions. The extrapolation is somewhat uncertain, which may explain the variety of boundary conditions used in the literature.
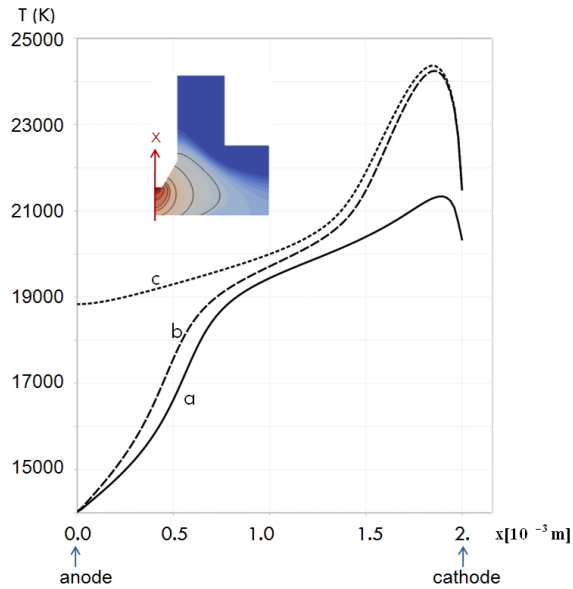
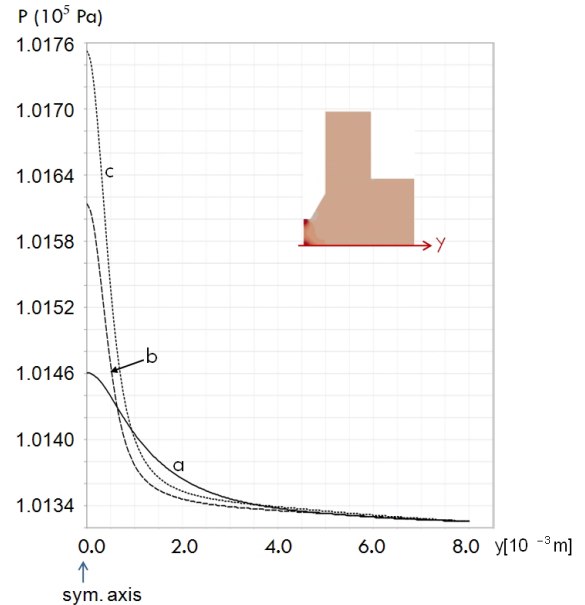**Figure 15: Influence of the anode and cathode boundary conditions on the temperature along the symmetry axis.**

Figure 17: Influence of the anode and cathode boundary conditions on the pressure on the base metal.
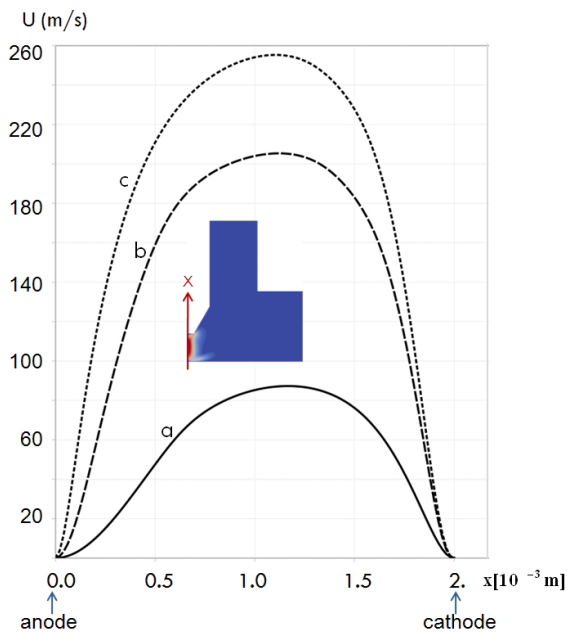

Figure 16: Influence of the anode and cathode boundary conditions on the velocity along the symmetry axis.

Three test cases (a, b, and c) that differ only by the boundary conditions set on the electrode and the anode were calculated to evaluate the influence of these boundary conditions on the plasma arc. In case a (treated above using the boundary conditions defined in [11]), the current density is uniform on the 0.5 mm radius cathode tip, and it decreases linearly down to zero as the radius tip increases. In case b all the current density (also uniform) goes through the 0.5 mm radius cathode tip. The boundary conditions on the anode are the same in case a and b. In case c the boundary conditions on the cathode are the same as in case b. Case c is associated with an extreme thermal condition on the anode for testing the model: its anode does not conduct heat. In all cases, argon is used as shielding gas.

The temperature and the velocity calculated for each case are plotted along the symmetry axis in Fig. 15 and Fig. 16, respectively; while the pressure on the base metal is plotted in Fig. 17.

It can be observed in Fig. 15 that there is a large influence of the current density distribution on the cathode on the maximum arc temperature. Also, compared to case a, the maximum temperature of case b is much closer to the maximum temperature observed

experimentaly. The thermal boundary condition on the anode has almost no influence on the maximum arc temperature. However, it can significantly affect the heat transferred to the anode base metal, as it significantly changes the temperature close to the anode.

Finally, Fig. 16 and 17 show that the velocity along the symmetry axis and the pressure force on the base metal are significantly changed for each variation tested on the anode and cathode boundary conditions.

4 CONCLUSION

This study focused on the modeling and simulation of an electric arc heat source in three space dimensions, coupling thermal fluid mechanics with electromagnetism. The model was implemented in the open source software OpenFOAM 1.6.x. Two approaches were considered for calculating the magnetic field $\vec{B}$: i) three-dimensional, and ii) axisymmetric.

The electromagnetic part of the solver was tested against analytic solution for an infinite electric rod. The solutions are in perfect agreement.

The complete solver was tested against experimental measurements for GTAW with argon shielding gas and an axisymmetric configuration. The numerical solutions for the $\vec{B}$-field then significantly differ. The axisymmetric approach indeed neglects the radial current density component. For axisymmetric configurations that are not invariant by translation along the symmetry axis, such as GTAW, this simplification is not everywhere justfified. Consequently, the axisymmetric approach, Eq. (6), was not retained for simulating the GTAW heat source. The numerical results obtained using the three-dimensional approach, Eqs. (4)-(5), show a good agreement with experimental data when such comparisions can be made.

Plasma arc simulations were done to evaluate qualitatively the influence of the amount of active gas on the plasma arc. The following Ar-x%CO_2 shielding gas compositions were used: pure argon (x=0), pure carbon dioxide (x=100), and mixtures of these two gases with x=1 and 10% in mole. The simulation results clearly show that the presence of carbon dioxide results in thermal arc constriction, and increased maximum arc temperature and velocity. The difficulty met in setting appropriate boundary conditions on the anode and cathode because of lack of experimental

data raises the future need of extending the simulation model coupling cathode and anode simulation to the thermal plasma arc.

Setting appropriate boundary conditions on the anode and cathode can also be a difficult issue even when experimental data are available. The freedom for extrapolating the boundary conditions can be rather large. In addition different possible conditions significantly affect the simulation results, such as the plasma arc temperature and velocity. Temperature and current density distribution on the electrode surface should thus be calculated rather than set, to enhance the predictive capability of the simulation model. Solution of the temperature and electromagnetic fields inside the anode and cathode, and the modeling of the plasma arc sheath doing the coupling with the plasma core, will thus be included in the forthcoming development of the simulation model.

5 References

[1] L. Lindgren, B. Babu, C. Charles, and D. Wedberg (2010). Simulation of manufacturing chains and use of coupled microtructure and constitutive models. *Finite Plasticity and Visco-plasticity of Conventional and Emerging Materials*, Khan, A. S. and B. Farrokh, (red.). NEAT PRESS, 4 s.

[2] A. Kumar, and T. DebRoy (2007). Heat transfer and fluid flow during Gas-Metal-Arc fillet welding for various joint configurations and welding positions. *The minerals, metals and materials society and ASM International*.

[3] J. Wendelstorf (2000). Ab initio modelling of thermal plasma gas discharges (electric arcs). PhD. Thesis, Carolo-Wilhelmina University, Germany.

[4] Y. Tanaka, T. Michishita and Y. Uesugi (2005). Hydrodynamic chemical non-equilibrium model of a pulsed arc discharge in dry air at atmospheric pressure. *Plasma Sources Sci. Technol.* **14**, pp. 134-151

[5] K. Yamamoto, M. Tanaka, S. Tashiro, K. Nakata, K. Yamazaki, E. Yamamoto, K. Suzuki, and A.B. Murphy (2008). Numerical simulation of metal vapor behavior in arc plasma. *Surface and Coatings Technology*, **202**, pp. 5302-5305.

[6] J. Hu, and L.S. Tsai (2007). Heat and mass transfer in gas metal arc welding. Part I: The arc, Part II: The metal. *International Journal of Heat and Mass Transfer* 50, pp. 808-820, 833-846.

[7] G. Xu, J. Hu and H.L. Tsai (2009). Three-dimensional modeling of arc plasma and metal transfer in gas metal arc welding. *International Journal of Heat and Mass Transfer*, **52**, pp. 1709-1724.

[8] I. Choquet, and B. Lucquin-Desreux (2011), Non equilibrium ionization in magnetized two-temperature thermal plasma, *Kinetic and Related Models*, **4**, to appear. (preprint www.ljll.math.upmc.fr/publications/2010/R10043.pdf)

[9] M. Sass-Tisovskaya (2009). *Plasma arc welding simulation with OpenFOAM*, Licentiate Thesis, Chalmers University of Technology, Gothenburg, Sweden.

[10] K.C. Hsu, K. Etemadi and E. Pfender (1983). Study of the free-burning high intensity argon arc, *J. Appl. Phys.*, **54**, pp. 1293-1301.

[11] M.C.Tsai, and Sindo Kou (1990). Heat transfer and fluid flow in welding arcs produced by sharpened and flat electrodes. *Int J. Heat Mass Transfer*, **33**, 10, pp. 2089-2098.

[12] V. Rat, A. Pascal, J. Aubreton, M.F. Elchinger, P. Fauchais and A. Lefort (2001). Transport properties in a two-temperature plasma: theory and application. *Physical Review E*, **64**, 026409.

[13] P. André, J. Aubreton, S. Clain , M. Dudeck, E. Duffour, M. F. Elchinger, B. Izrar, D. Rochette, R. Touzani, and D. Vacher (2010), Transport coefficients in thermal plasma. Applications to Mars and Titan atmospheres, *European Physical Journal D 57*, **2**, pp. 227-234.

[14] G.N. Haddad, and A.J.D. Farmer (1985) Temperature measurements in gas tungsten Arcs. *Welding Journal* **24**, pp. 339-342.

[15] I. Choquet, H, Nilsson, M. Sass-Tisovskaya (2011). Modeling and simulation of a heat source in electric welding, *In Proc. Swedish Production Symposium, SPS11*, May 3-5, 2011, Lund, Sweden. *to appear*.

[16] R.E. Sonntag, C. Borgnakke, and G.J. Van Wylen (2003). *Fundamentals of thermodynamics*, Wiley, 6th edition.

[17] R. J. Kee, M. E. Coltrin, P. Glaborg (2003). *Chemically reacting flow. Theory and Practice*, Wiley Interscience.